

Measurement of the Hadronic Decay Current in $\tau^- \rightarrow \pi^- \pi^- \pi^+ \nu_\tau$

The OPAL Collaboration

Abstract

The decay $\tau^- \rightarrow \pi^- \pi^- \pi^+ \nu_\tau$ has been studied using data collected with the OPAL detector at LEP during 1992 and 1993. The hadronic structure functions for this decay are measured model independently assuming G-parity invariance and neglecting scalar currents. Simultaneously the parity violating asymmetry parameter is determined to be $\gamma_{VA} = 1.08^{+0.46}_{-0.41} {}^{+0.14}_{-0.25}$, consistent with the Standard Model prediction of $\gamma_{VA} = 1$ for left-handed tau neutrinos. Models of Kühn and Santamaria and of Isgur et al. are used to fit distributions of the invariant 3π mass as well as 2π mass projections of the Dalitz plot. The model dependent mass and width of the a_1 resonance are measured to be $m_{a_1} = 1.266 \pm 0.014^{+0.012}_{-0.002}$ GeV and $\Gamma_{a_1} = 0.610 \pm 0.049^{+0.053}_{-0.019}$ GeV for the Kühn and Santamaria model and $m_{a_1} = 1.202 \pm 0.009^{+0.009}_{-0.001}$ GeV and $\Gamma_{a_1} = 0.422 \pm 0.023^{+0.033}_{-0.004}$ GeV for the Isgur et al. model. The model dependent values obtained for the parity violating asymmetry parameter are $\gamma_{VA} = 0.87 \pm 0.27^{+0.05}_{-0.06}$ for the Kühn and Santamaria model and $\gamma_{VA} = 1.10 \pm 0.31^{+0.13}_{-0.14}$ for the Isgur et al. model. Within the Isgur et al. model the ratio of the S - and D -wave amplitudes is measured to be $D/S = -0.09 \pm 0.03 \pm 0.01$.

(to be submitted to Zeit. f. Physik)

R. Akers¹⁶, G. Alexander²³, J. Allison¹⁶, K. Ametewee²⁵, K.J. Anderson⁹, S. Arcelli²,
 S. Asai²⁴, D. Axen²⁹, G. Azuelos^{18,a}, A.H. Ball¹⁷, E. Barberio²⁶, R.J. Barlow¹⁶, R. Bartoldus³,
 J.R. Batley⁵, G. Beaudoin¹⁸, A. Beck²³, G.A. Beck¹³, C. Beeston¹⁶, T. Behnke²⁷, K.W. Bell²⁰,
 G. Bella²³, S. Bentvelsen⁸, P. Berlich¹⁰, S. Bethke³², O. Biebel³², I.J. Bloodworth¹, P. Bock¹¹,
 H.M. Bosch¹¹, M. Boutemur¹⁸, S. Braibant¹², P. Bright-Thomas²⁵, R.M. Brown²⁰, A. Buijs⁸,
 H.J. Burckhart⁸, R. Bürgin¹⁰, C. Burgard²⁷, N. Capdevielle¹⁸, P. Capiluppi², R.K. Carnegie⁶,
 A.A. Carter¹³, J.R. Carter⁵, C.Y. Chang¹⁷, C. Charlesworth⁶, D.G. Charlton^{1,b}, S.L. Chu⁴,
 P.E.L. Clarke¹⁵, J.C. Clayton¹, S.G. Clowes¹⁶, I. Cohen²³, J.E. Conboy¹⁵, O.C. Cooke¹⁶,
 M. Cuffiani², S. Dado²², C. Dallapiccola¹⁷, G.M. Dallavalle², C. Darling³¹, S. De Jong¹²,
 L.A. del Pozo⁸, H. Deng¹⁷, M. Dittmar⁴, M.S. Dixit⁷, E. do Couto e Silva¹², J.E. Duboscq⁸,
 E. Duchovni²⁶, G. Duckeck⁸, I.P. Duerdoth¹⁶, U.C. Dunwoody⁵, J.E.G. Edwards¹⁶,
 P.A. Elcombe⁵, P.G. Estabrooks⁶, E. Etzion²³, H.G. Evans⁹, F. Fabbri², B. Fabbro²¹,
 M. Fanti², P. Fath¹¹, M. Fierro², M. Fincke-Keeler²⁸, H.M. Fischer³, P. Fischer³, R. Folman²⁶,
 D.G. Fong¹⁷, M. Foucher¹⁷, H. Fukui²⁴, A. Fürtjes⁸, P. Gagnon⁶, A. Gaidot²¹, J.W. Gary⁴,
 J. Gascon¹⁸, N.I. Geddes²⁰, C. Geich-Gimbel³, S.W. Gensler⁹, F.X. Gentit²¹, T. Gerasis²⁰,
 G. Giacomelli², P. Giacomelli⁴, R. Giacomelli², V. Gibson⁵, W.R. Gibson¹³, J.D. Gillies²⁰,
 J. Goldberg²², D.M. Gingrich^{30,a}, M.J. Goodrick⁵, W. Gorn⁴, C. Grandi², E. Gross²⁶,
 J. Hagemann²⁷, G.G. Hanson¹², M. Hansroul⁸, C.K. Hargrove⁷, P.A. Hart⁹, M. Hauschild⁸,
 C.M. Hawkes⁸, E. Heflin⁴, R.J. Hemingway⁶, G. Herten¹⁰, R.D. Heuer⁸, J.C. Hill⁵,
 S.J. Hillier⁸, T. Hilse¹⁰, P.R. Hobson²⁵, D. Hochman²⁶, R.J. Homer¹, A.K. Honma^{28,a},
 R. Howard²⁹, R.E. Hughes-Jones¹⁶, P. Igo-Kemenes¹¹, D.C. Imrie²⁵, A. Jawahery¹⁷,
 P.W. Jeffreys²⁰, H. Jeremie¹⁸, M. Jimack¹, M. Jones⁶, R.W.L. Jones⁸, P. Jovanovic¹, C. Jui⁴,
 D. Karlen⁶, J. Kanzaki²⁴, K. Kawagoe²⁴, T. Kawamoto²⁴, R.K. Keeler²⁸, R.G. Kellogg¹⁷,
 B.W. Kennedy²⁰, B. King⁸, J. King¹³, J. Kirk²⁹, S. Kluth⁵, T. Kobayashi²⁴, M. Kobel¹⁰,
 D.S. Koetke⁶, T.P. Kokott³, S. Komamiya²⁴, R. Kowalewski⁸, T. Kress¹¹, P. Krieger⁶, J. von
 Krogh¹¹, P. Kyberd¹³, G.D. Lafferty¹⁶, H. Lafoux⁸, R. Lahmann¹⁷, W.P. Lai¹⁹, J. Lauber⁸,
 J.G. Layter⁴, P. Leblanc¹⁸, A.M. Lee³¹, E. Lefebvre¹⁸, D. Lellouch²⁶, C. Leroy¹⁸, J. Letts²,
 L. Levinson²⁶, S.L. Lloyd¹³, F.K. Loebinger¹⁶, G.D. Long¹⁷, B. Lorazo¹⁸, M.J. Losty⁷,
 X.C. Lou⁸, J. Ludwig¹⁰, A. Luig¹⁰, M. Mannelli⁸, S. Marcellini², C. Markus³, A.J. Martin¹³,
 J.P. Martin¹⁸, T. Mashimo²⁴, W. Matthews²⁵, P. Mättig³, U. Maur³, J. McKenna²⁹,
 T.J. McMahon¹, A.I. McNab¹³, F. Meijers⁸, F.S. Merritt⁹, H. Mes⁷, A. Michelini⁸,
 R.P. Middleton²⁰, G. Mikenberg²⁶, D.J. Miller¹⁵, R. Mir²⁶, W. Mohr¹⁰, A. Montanari²,
 T. Mori²⁴, M. Morii²⁴, U. Müller³, B. Nellen³, B. Nijhar¹⁶, S.W. O'Neale¹, F.G. Oakham⁷,
 F. Odorici², H.O. Ogren¹², N.J. Oldershaw¹⁶, C.J. Oram^{28,a}, M.J. Oreglia⁹, S. Orito²⁴,
 F. Palmonari², J.P. Pansart²¹, G.N. Patrick²⁰, M.J. Pearce¹, P.D. Phillips¹⁶, J.E. Pilcher⁹,
 J. Pinfold³⁰, D.E. Plane⁸, P. Poffenberger²⁸, B. Poli², A. Posthaus³, T.W. Pritchard¹³,
 H. Przysiezniak³⁰, M.W. Redmond⁸, D.L. Rees⁸, D. Rigby¹, M.G. Rison⁵, S.A. Robins¹³,
 D. Robinson⁵, N. Rodning³⁰, J.M. Roney²⁸, E. Ros⁸, A.M. Rossi², M. Rosvick²⁸,
 P. Routenburg³⁰, Y. Rozen⁸, K. Runge¹⁰, O. Runolfsson⁸, D.R. Rust¹², M. Sasaki²⁴,
 C. Sbarra², A.D. Schaile⁸, O. Schaile¹⁰, F. Scharf³, P. Scharff-Hansen⁸, P. Schenk⁴,
 B. Schmitt³, M. Schröder⁸, H.C. Schultz-Coulon¹⁰, P. Schütz³, M. Schulz⁸, C. Schwick²⁷,
 J. Schwiening³, W.G. Scott²⁰, M. Settles¹², T.G. Shears⁵, B.C. Shen⁴,
 C.H. Shepherd-Themistocleous⁷, P. Sherwood¹⁵, G.P. Siroli², A. Skillman¹⁵, A. Skuja¹⁷,
 A.M. Smith⁸, T.J. Smith²⁸, G.A. Snow¹⁷, R. Sobie²⁸, S. Söldner-Rembold¹⁰, R.W. Springer³⁰,
 M. Sproston²⁰, A. Stahl³, M. Starks¹², C. Stegmann¹⁰, K. Stephens¹⁶, J. Steuerer²⁸,
 B. Stockhausen³, D. Strom¹⁹, P. Szymanski²⁰, R. Tafirout¹⁸, H. Takeda²⁴, T. Takeshita²⁴,
 P. Taras¹⁸, S. Tarem²⁶, M. Tecchio⁹, P. Teixeira-Dias¹¹, N. Tesch³, M.A. Thomson⁸,

O. Tousignant¹⁸, S. Towers⁶, M. Tscheulin¹⁰, T. Tsukamoto²⁴, A.S. Turcot⁹,
M.F. Turner-Watson⁸, P. Utzat¹¹, R. Van Kooten¹², G. Vasseur²¹, P. Vikas¹⁸, M. Vinciter²⁸,
A. Wagner²⁷, D.L. Wagner⁹, C.P. Ward⁵, D.R. Ward⁵, J.J. Ward¹⁵, P.M. Watkins¹,
A.T. Watson¹, N.K. Watson⁷, P. Weber⁶, P.S. Wells⁸, N. Wermes³, B. Wilkens¹⁰,
G.W. Wilson²⁷, J.A. Wilson¹, V-H. Winterer¹⁰, T. Wlodek²⁶, G. Wolf²⁶, S. Wotton¹¹,
T.R. Wyatt¹⁶, A. Yeaman¹³, G. Yekutieli²⁶, M. Yurko¹⁸, V. Zacek¹⁸, W. Zeuner⁸, G.T. Zorn¹⁷.

¹School of Physics and Space Research, University of Birmingham, Birmingham B15 2TT, UK

²Dipartimento di Fisica dell' Università di Bologna and INFN, I-40126 Bologna, Italy

³Physikalisches Institut, Universität Bonn, D-53115 Bonn, Germany

⁴Department of Physics, University of California, Riverside CA 92521, USA

⁵Cavendish Laboratory, Cambridge CB3 0HE, UK

⁶Carleton University, Department of Physics, Colonel By Drive, Ottawa, Ontario K1S 5B6, Canada

⁷Centre for Research in Particle Physics, Carleton University, Ottawa, Ontario K1S 5B6, Canada

⁸CERN, European Organisation for Particle Physics, CH-1211 Geneva 23, Switzerland

⁹Enrico Fermi Institute and Department of Physics, University of Chicago, Chicago IL 60637, USA

¹⁰Fakultät für Physik, Albert Ludwigs Universität, D-79104 Freiburg, Germany

¹¹Physikalisches Institut, Universität Heidelberg, D-69120 Heidelberg, Germany

¹²Indiana University, Department of Physics, Swain Hall West 117, Bloomington IN 47405, USA

¹³Queen Mary and Westfield College, University of London, London E1 4NS, UK

¹⁵University College London, London WC1E 6BT, UK

¹⁶Department of Physics, Schuster Laboratory, The University, Manchester M13 9PL, UK

¹⁷Department of Physics, University of Maryland, College Park, MD 20742, USA

¹⁸Laboratoire de Physique Nucléaire, Université de Montréal, Montréal, Quebec H3C 3J7, Canada

¹⁹University of Oregon, Department of Physics, Eugene OR 97403, USA

²⁰Rutherford Appleton Laboratory, Chilton, Didcot, Oxfordshire OX11 0QX, UK

²¹CEA, DAPNIA/SPP, CE-Saclay, F-91191 Gif-sur-Yvette, France

²²Department of Physics, Technion-Israel Institute of Technology, Haifa 32000, Israel

²³Department of Physics and Astronomy, Tel Aviv University, Tel Aviv 69978, Israel

²⁴International Centre for Elementary Particle Physics and Department of Physics, University of Tokyo, Tokyo 113, and Kobe University, Kobe 657, Japan

²⁵Brunel University, Uxbridge, Middlesex UB8 3PH, UK

²⁶Particle Physics Department, Weizmann Institute of Science, Rehovot 76100, Israel

²⁷Universität Hamburg/DESY, II Institut für Experimental Physik, Notkestrasse 85, D-22607 Hamburg, Germany

²⁸University of Victoria, Department of Physics, P O Box 3055, Victoria BC V8W 3P6, Canada

²⁹University of British Columbia, Department of Physics, Vancouver BC V6T 1Z1, Canada

³⁰University of Alberta, Department of Physics, Edmonton AB T6G 2J1, Canada

³¹Duke University, Dept of Physics, Durham, NC 27708-0305, USA

³²Technische Hochschule Aachen, III Physikalisches Institut, Sommerfeldstrasse 26-28, D-52056 Aachen, Germany

^aAlso at TRIUMF, Vancouver, Canada V6T 2A3

^b Royal Society University Research Fellow

1 Introduction

The τ lepton is the only lepton massive enough to decay into hadrons. It therefore offers an ideal laboratory to study the weak hadronic current under clean conditions. The decay $\tau^- \rightarrow \pi^- \pi^- \pi^+ \nu_\tau$ ¹ is dominated by the a_1 resonance $\tau^- \rightarrow a_1^- \nu_\tau$ followed by the subsequent decay $a_1^- \rightarrow \pi^- \pi^- \pi^+$ through the decay chain $a_1^- \rightarrow \rho^0 \pi^-$ and $\rho^0 \rightarrow \pi^+ \pi^-$. Several aspects of the $\tau^- \rightarrow \pi^- \pi^- \pi^+ \nu_\tau$ decay have already been studied [1-3]. All of these studies require a detailed understanding of the properties of the a_1 resonance or, more generally, the structure of the hadronic decay current in $\tau^- \rightarrow \pi^- \pi^- \pi^+ \nu_\tau$.

In this paper, we present two different approaches for determining the structure of the decay $\tau^- \rightarrow \pi^- \pi^- \pi^+ \nu_\tau$. In the first approach, a model independent analysis is used to extract the structure of the weak hadronic current using a general description of hadronic τ decays as proposed by Kühn and Mirkes [4]. The parity violating asymmetry parameter γ_{VA} can also be measured within this framework. In the second approach, the models of Kühn and Santamaria [5] and of Isgur et al. [6] are used for comparison with the OPAL data. Values for the a_1 mass and width are extracted. In the Isgur et al. model, the ratio of the amplitudes of the two possible intermediate $\rho\pi$ angular momentum states (the D/S ratio) is also extracted. In addition both models are used to measure γ_{VA} model dependently.

A brief description of the OPAL detector is given in section 2. The data selection, based on a likelihood method, is described in section 3. The theoretical framework of the $\tau^- \rightarrow \pi^- \pi^- \pi^+ \nu_\tau$ decay is presented in section 4 followed by the measurement of the model independent structure functions and the parity violating asymmetry parameter γ_{VA} in section 5. Section 6 is devoted to the model dependent description of the decay. An introduction and comparison of the two models are given. In section 7 the a_1 resonance parameters m_{a_1} , Γ_{a_1} , and the D/S ratio are extracted. The measured structure functions are compared to the model predictions and model dependent values of γ_{VA} are determined. Finally, the results are summarized in section 8.

2 The OPAL Detector

The OPAL detector at LEP is described in detail elsewhere [7]. Therefore only the most important elements for this analysis, the tracking system and the electromagnetic calorimeter, are briefly introduced.

The innermost detector for the measurement of charged tracks is a silicon microvertex detector with planes at radii of 6.1 and 7.5 cm. Moving further from small to large radius, the central tracking system consists of a precision vertex drift chamber with 12 axial wires and 6 small angle stereo wires extending in radius from about 10 to 21 cm, a 4 m long by 3.7 m diameter drift chamber (jet-chamber) with 159 layers of axial anode wires providing a momentum resolution of $\sigma_p/p^2 = 2.2 \times 10^{-3} \text{ GeV}^{-1}$ [8], and z -chambers which provide up to six precise measurements of the z -coordinate of charged particles. The whole central tracking detector is immersed in a 0.435 T axial magnetic field. The jet-chamber also provides measurements of the specific energy loss of tracks in gas (dE/dx).

The electromagnetic energy is measured by a detector composed of lead-glass blocks located outside the magnetic coil. Each block covers approximately $40 \times 40 \text{ mrad}^2$. The

¹References in this paper to specific charge states apply to the charge conjugate states also.

depth of the calorimeter material is 24.6 radiation lengths. For the considered $\cos\theta$ range of this analysis ($|\cos\theta| < 0.68$) the electromagnetic calorimeter has a time-of-flight detector and a preshower system (presampler) consisting of limited streamer tubes in front of the lead-glass blocks.

3 Selection of $\tau^- \rightarrow \pi^- \pi^- \pi^+ \nu_\tau$ Decays

The standard OPAL τ pair selection [9] has been applied to the data. The topology of $e^+e^- \rightarrow \tau^+\tau^-$ events is characterized by a pair of back-to-back, narrow jets with low particle multiplicity. Tracks and electromagnetic clusters are grouped into cones of 35° half opening angle where each cone is assumed to contain the decay products of one of the τ leptons.

A number of background sources in the τ pair selection have to be considered. $Z^0 \rightarrow q\bar{q}$ events are removed by requiring at least two, but not more than six tracks which have passed standard quality cuts and not more than ten clusters in the electromagnetic calorimeter. Background from two photon events, $e^+e^- \rightarrow (e^+e^-)X$, is removed by cuts on the visible energy and the acollinearity. Cosmic ray background is suppressed mainly by requirements on the time-of-flight. The background from lepton pairs, $e^+e^- \rightarrow e^+e^-$ and $e^+e^- \rightarrow \mu^+\mu^-$, is removed by cuts on the momenta, the energy deposited in the electromagnetic calorimeter, and signals in the muon chambers.

A total of 57397 events from the 1992 and 1993 data sets pass this τ pair selection, with an estimated non τ pair background of $(1.83 \pm 0.30)\%$ [10].

From this sample $\tau^- \rightarrow h^- h^- h^+ \nu_\tau$ candidates (with h being either a π or K) are selected. Three charged tracks are required in a cone with the absolute sum of the charges to be 1. The axis of the cone has to lie within $|\cos\theta_{cone}| < 0.68$ to achieve the best possible angular resolution. The scaled charged momentum $x_{cone} = \sum_{i=1}^3 p_i/E_{beam}$ of the cone has to be larger than 0.05. The remaining cones are then subjected to a channel likelihood method [11] to identify the decay $\tau^- \rightarrow h^- h^- h^+ \nu_\tau$.

The main background sources for the $\tau^- \rightarrow h^- h^- h^+ \nu_\tau$ decay are τ decays to one charged particle accompanied by a photon undergoing a conversion to an e^+e^- pair, and the decay $\tau^- \rightarrow h^- h^- h^+ \geq 1$ neutrals ν_τ . Efficiency and backgrounds for the following analysis are calculated assuming branching ratios of $(8.42 \pm 0.31)\%$ for the $\tau^- \rightarrow h^- h^- h^+ \nu_\tau$ decay and $(5.63 \pm 0.30)\%$ for the $\tau^- \rightarrow h^- h^- h^+ \geq 1$ neutrals ν_τ decay [12]. Tracks from photon conversions do not in general point back to the decay vertex of the τ lepton and they can often be identified as electrons by their energy loss in the central jet chamber. In the case of a π^0 Dalitz decay electron identification is the only way to reject this background. A surplus of energy in the electromagnetic calorimeter compared to the momentum of the tracks or additional neutral clusters in the presampler in front of the electromagnetic calorimeter might also indicate the presence of photons in the cone. Four variables are thus used for the likelihood selection:

- For each of the three tracks i ($i = 1, 2, 3$) in a cone the probability that the measured energy loss is consistent with that expected for an electron $P_i(e)$ and a pion $P_i(\pi)$ is calculated. The probability of all three particles being pions is defined to be:

$$\text{Prob}_{3\pi} = \frac{P_1(\pi^-) P_2(\pi^-) P_3(\pi^+)}{P_1(\pi^-) P_2(\pi^-) P_3(\pi^+) + P_1(\pi^-) P_2(e^-) P_3(e^+) + P_1(e^-) P_2(\pi^-) P_3(e^+)}.$$

- The three tracks are fitted to a common vertex in the plane perpendicular to the beam. The χ^2 measures the probability that the three tracks have the same origin.
- The energy deposited in the electromagnetic calorimeter of the entire cone ($\sum E$) is divided by the scalar sum of the momenta of the three charged tracks measured in the tracking chambers ($\sum p$).
- The multiplicities of all clusters in the presampler detector which are at least 20 mrad away from the impact point of any of the three charged tracks are summed up.

For the Monte Carlo simulation we have used KORALZ 4.0 [13] with TAUOLA 2.4 [14] to generate the τ leptons and model their decays. This is followed by a full simulation of the OPAL detector [15]. In TAUOLA, the decay $\tau^- \rightarrow \pi^- \pi^- \pi^+ \nu_\tau$ is given by the model of Kühn and Santamaria [5]. The Monte Carlo sample contains approximately four times as many events as the data sample.

To check the agreement between data and Monte Carlo, reference samples have been selected for each of the four variables by applying stringent cuts on the three variables not under examination. Two examples for the comparison between data events and Monte Carlo simulated events are shown in fig. 1 and 2. The overall agreement is satisfactory. The systematic uncertainty due to small differences observed between the data and Monte Carlo samples is estimated to be 0.03 for the efficiency and 0.01 for the purity.

The selected sample of $\tau^- \rightarrow h^- h^- h^+ \nu_\tau$ decays contains events where one or more of the three hadrons are kaons. The measurement of the energy loss in the jet chamber is used to reject these events. The probability that all three hadrons are pions is compared to the sum of the probabilities for any combination of pions and kaons. A cut is applied on the three-pion-probability-ratio at 0.05.

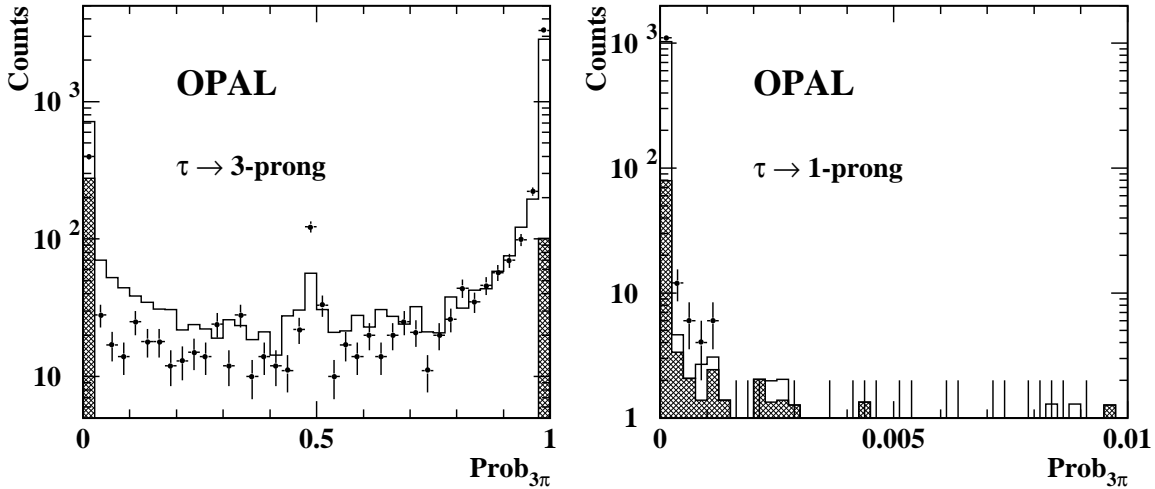


Figure 1: Distributions of $\text{Prob}_{3\pi}$ for data (points with error bars), Monte Carlo (solid line), and Monte Carlo background events (hatched area). No attempt has been made to distinguish between $\tau^- \rightarrow h^- h^- h^+ \nu_\tau$ and $\tau^- \rightarrow \pi^- \pi^- \pi^+ \pi^0 \nu_\tau$ in the 3-prong sample.

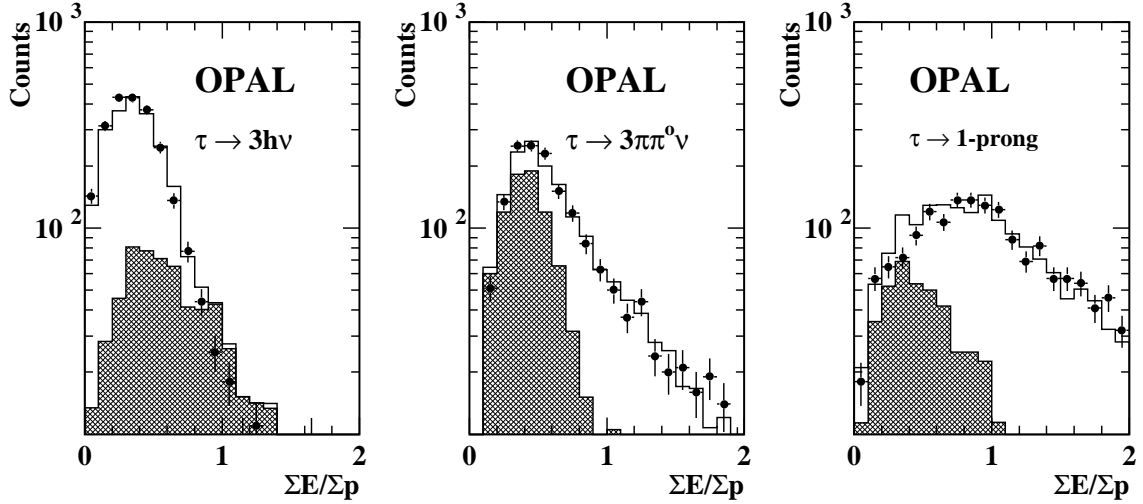


Figure 2: Distributions of $\Sigma E/\Sigma p$ for data (points with error bars), Monte Carlo (line) and Monte Carlo background events (hatched area).

To improve the momentum resolution in the final sample all tracks are constrained to the τ decay vertex from the vertex fit and the 3-momenta of the tracks are reevaluated. Pion masses are assumed when calculating the energy of the three particles. Badly reconstructed events are rejected by removing events with a low χ^2 probability of the vertex fit ($Prob(\chi^2) > 0.02$) and by requiring hits in the z -chambers for all three tracks. These two very restrictive cuts further reduce the efficiency. However, they guarantee an accurate kinematic reconstruction of the events. Only events with an invariant mass squared of the hadronic system between 0.5 and 2.75 GeV^2 are used in the analyses, rejecting 0.4% of the $\tau^- \rightarrow \pi^- \pi^- \pi^+ \nu_\tau$ decays according to Monte Carlo simulated events. The overall efficiency is 18.5% and shows only little dependence on the kinematic variables. The final data sample consists of 2585 events, with an estimated purity of $(82.5 \pm 0.4)\%$ $\tau^- \rightarrow \pi^- \pi^- \pi^+ \nu_\tau$ events. Estimated contributions of the individual background channels are itemized in table 1. A conventional cut method has been used as a cross check to the channel likelihood selection.

decay channel	background fraction
$\tau^- \rightarrow \pi^- \pi^- \pi^+ \pi^0 \nu_\tau$	$(15.1 \pm 0.4)\%$
$\tau^- \rightarrow K^- \pi^- \pi^+ \nu_\tau$	$(1.2 \pm 0.1)\%$
$\tau^- \rightarrow \pi^- K^- K^+ \nu_\tau$	$(0.5 \pm 0.1)\%$
$\tau^- \rightarrow \pi^- \pi^- \pi^+ 2\pi^0 \nu_\tau$	$(0.5 \pm 0.1)\%$
others	$(0.2 \pm 0.1)\%$

Table 1: Estimated background fractions in the final data sample. The errors are statistical only.

4 Theoretical Description of the Decay

The partial decay width of the decay $\tau^- \rightarrow \pi^- \pi^- \pi^+ \nu_\tau$ can be written as ²

$$d\Gamma(\tau^- \rightarrow \pi^- \pi^- \pi^+ \nu_\tau) = \sum_{\mu\nu} \frac{G_F^2}{4m_\tau} \cos^2 \theta_C L_{\mu\nu} H^{\mu\nu} d\text{PS}^{(4)}. \quad (1)$$

G_F is the Fermi constant, θ_C the Cabbibo angle, m_τ is the mass of the τ lepton and $d\text{PS}^{(4)}$ symbolizes the phase space integration. The leptonic tensor $L_{\mu\nu}$ can be calculated from electroweak theory and $H^{\mu\nu}$ is the hadronic tensor, the subject of our measurement.

Kühn and Mirkes [4] have recently proposed to expand the product of the leptonic and hadronic tensors in eq. (1) in a sum of 16 independent terms,

$$\sum_{\mu\nu} L_{\mu\nu} H^{\mu\nu} = 2(m_\tau^2 - Q^2) \sum_X L_X W_X. \quad (2)$$

The L_X are symmetric and antisymmetric combinations of the $L_{\mu\nu}$ components. The terms W_X are called hadronic structure functions. They depend on the four-momenta of the outgoing pions in a Lorentz invariant way, that is, $W_X \equiv W_X(s_1, s_2, Q^2)$. Q^2 is the mass squared of the hadronic system and s_1 and s_2 are the Dalitz plot variables. They are defined in terms of the pion momenta as $s_1 = (p_2 + p_3)^2$ and $s_2 = (p_1 + p_3)^2$, with the labels chosen such that $|\vec{p}_2| > |\vec{p}_1|$ for the two like-sign pions and p_3 refers to the unlike-sign pion. We will not determine the dependence of the structure functions on s_1 and s_2 due to limited statistics. Instead we define the structure functions $w_X(Q^2)$, integrated over the Dalitz plot variables s_1, s_2

$$w_X(Q^2) = \int W_X(s_1, s_2, Q^2) ds_1 ds_2. \quad (3)$$

Assuming G-parity invariance and neglecting scalar currents, which are expected to be small [2], the number of non-vanishing structure functions is reduced from sixteen to four ³, labeled w_A, w_C, w_D and w_E , following ref. [4]. w_A is the decay rate for an unpolarized transverse virtual W-boson with helicity axis along the normal to the hadronic decay plane. The two structure functions w_C and w_D are combinations of the interference terms of the helicity +1 and -1 amplitudes and w_E measures the difference of these two helicity states.

The detailed forms of the L_X are given in appendix A. They can be calculated within the framework of the electroweak theory as functions of the τ polarisation \mathbf{P}_τ , the parity violating asymmetry parameter γ_{VA} ($\gamma_{VA} = 2g_V g_A / (g_V^2 + g_A^2) = 1$ in the Standard Model), the invariant mass squared of the hadronic system Q^2 , and four decay angles [4] defined below.

The Gottfried–Jackson angle θ^* [16] is the angle of the direction of the hadronic system \vec{n}_Q with respect to the τ line of flight in the τ rest frame (shown schematically in fig. 3). To define the line of flight of the τ in its own rest frame the inverse of the boost direction (\vec{n}_b) is taken. The value of $\cos \theta^*$ is determined from the total energy of the three pions and their invariant mass. The three Euler angles α, β , and γ describe the orientation of the hadronic system (\vec{n}_Q) with respect to the laboratory system, defined by the τ direction, as seen from the hadronic rest frame. In this analysis we integrate over α as the direction of flight of the

²Throughout this paper, units are chosen such that $\hbar = c = 1$.

³For example $w_B = 0$ due to G-parity conservation and $w_{SA} = 0$ because scalar currents are neglected.

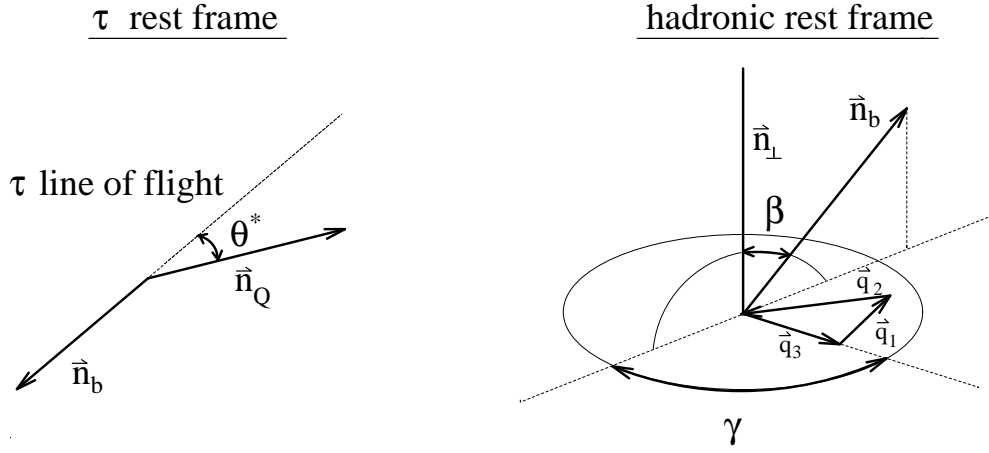


Figure 3: Schematic view of the angles θ^* in the τ rest frame (left) and β and γ in the hadronic rest frame (right).

τ has to be known for its reconstruction. The angles β and γ can be determined from the momenta of the three pions. β is the angle between the normal to the hadronic decay plane \vec{n}_\perp and the boost direction \vec{n}_b (see fig. 3). The angle γ determines the orientation of the three pions within their decay plane. A reference direction is given by the projection of \vec{n}_b onto the decay plane. γ is the angle between the direction of the unlike-sign pion (the π^+ for a τ^- decay) with respect to this reference direction.

5 Extraction of the Structure Functions

The hadronic structure functions w_A , w_C , w_D and w_E have been determined for the decay $\tau^- \rightarrow \pi^- \pi^- \pi^+ \nu_\tau$ in nine equal sized Q^2 bins between 0.5 and 2.75 GeV^2 . An extended maximum likelihood fit [17] is applied to the events for each Q^2 bin. The kinematic variables Q^2 , $\cos \theta^*$, $\cos \beta$ and γ are represented by z and $dz = dQ^2 d \cos \theta^* d \cos \beta d\gamma$, so the likelihood function is

$$(\ln \mathcal{L})_j = \sum_i^{N_j} \ln \left(\frac{d\Gamma}{dz} (z_i; w_A^j, w_C^j, w_D^j, w_E^j) \frac{N}{C_{corr} \Gamma_{3\pi}} \right) - \Gamma_{\Delta Q_j^2} (w_A^j) \frac{N}{C_{corr} \Gamma_{3\pi}}. \quad (4)$$

Here the w_X^j (with X either A , C , D or E) are the average values of the structure functions w_X within bin number j . They are the parameters of the fit. N_j is the number of events in bin number j whereas N is the total number of selected events. $\Gamma_{3\pi}$ is the partial decay width of the τ into three pions calculated from ref. [12] ($\Gamma_{3\pi}/\Gamma_{tot} = 7.98\%$, $\Gamma_{3\pi} = 1.78 \cdot 10^{-4} \text{eV}$). The factor C_{corr} (with $C_{corr} = 0.996$, see section 3) corrects $\Gamma_{3\pi}$ for events with $Q^2 < 0.5 \text{GeV}^2$ or $Q^2 > 2.75 \text{GeV}^2$. The decay distribution $d\Gamma/dz$ defined in eq. (1) is given by

$$\frac{d\Gamma}{dz} (z; w_X) = \frac{G_F^2}{512 m_\tau (2\pi)^6} \cos^2 \theta_C \{L_A w_A + L_C w_C + L_D w_D + L_E w_E\} \frac{(m_\tau^2 - Q^2)^2}{m_\tau^2 Q^2}. \quad (5)$$

The statistical factor 1/2 for the two identical pions in the final state is taken into account in the w_X . The normalization term $\Gamma_{\Delta Q^2}$ is the integral over the full ranges of the kinematic

angles, but Q^2 is only integrated over its respective bin width. It is given by

$$\begin{aligned}\Gamma_{\Delta Q^2} &= \int \frac{d\Gamma}{dz}(z; w_X) dz \\ &= \frac{G_F^2 \cos^2 \theta_C}{16\pi m_\tau^3} \frac{1}{3} \frac{1}{(4\pi)^4} \int_{Q_{min}^2}^{Q_{max}^2} \frac{1}{Q^4} (m_\tau^2 - Q^2)^2 (m_\tau^2 + 2Q^2) w_A dQ^2.\end{aligned}\quad (6)$$

Note that w_C , w_D and w_E vanish when integrated over the angles, so that $\Gamma_{\Delta Q^2}$ depends only on w_A .

The detector resolution has been taken into account by applying a smearing function to each of the kinematic variables on an event by event basis. The resolutions, determined from Monte Carlo simulated events, are found to be flat in the kinematic variables Q^2 , $\cos \theta^*$, $\cos \beta$ and γ and are independent of the scattering angles of the tracks. The detector resolution estimated from Monte Carlo has been cross checked by comparing samples from data and Monte Carlo of $e^+e^- \rightarrow e^+e^- \gamma$ events in which the photon has converted into an e^+e^- pair, for which the distributions of the angles $\cos \beta$ and γ show a distinct peak.

A smooth efficiency correction derived from Monte Carlo is incorporated in the fit by multiplying $d\Gamma/dz$ by a correction function for each of the four kinematic variables. It also includes a bin to bin correction for migration effects between neighbouring Q^2 bins.

The background is included in the fit by replacing $d\Gamma/dz$ in eq. (4) and (6) by

$$f_{sig} \frac{d\Gamma}{dz}(z; w_X) + f_{bgd} \frac{d\Gamma}{dz}(z; w_X^{bgd}) \quad (7)$$

where f_{sig} and f_{bgd} are the overall fractions of signal and background (see section 3) and w_X^{bgd} are the structure functions of the background. We assume that our formalism using the four structure functions as fit parameters also describes the background events. Note that the w_X^{bgd} do not have any physical meaning but are merely used for appropriate background parametrization. The w_X^{bgd} are obtained by running Monte Carlo simulated background events which have passed the signal selection cuts through the fit formalism given in eq. (4) replacing w_X by w_X^{bgd} .

5.1 Results

The hadronic structure functions are presented in fig. 4 and table 2. Only the statistical errors are shown in fig. 4. The lowest bin in the Q^2 distribution is dominated by background events (see fig. 6). It is therefore excluded from table 2 and only given as a cross check in fig. 4.

The uncertainty in the background dominates the systematic error. The different contributions have been estimated in the following way. The background fraction f_{bgd} has been changed in the fit by 0.02. The cut against 3-prong events with kaons was removed and half of the change is quoted as error. When compared to the uncertainty in the related branching ratios this leads to a conservative estimate. To derive the uncertainty from the background description the change from varying the background structure functions w_X^{bgd} within their statistical errors and half of the change obtained when using TAUOLA 1.5⁴ [18] instead of TAUOLA 2.4 [14] for the description of the background is added in quadrature.

⁴In version 1.5 the decay $\tau^- \rightarrow \pi^- \pi^- \pi^+ \pi^0 \nu_\tau$, which is the dominant background channel, is implemented in an oversimplified way. In version 2.5 subresonances have been included according to recent measurements [19, 20].

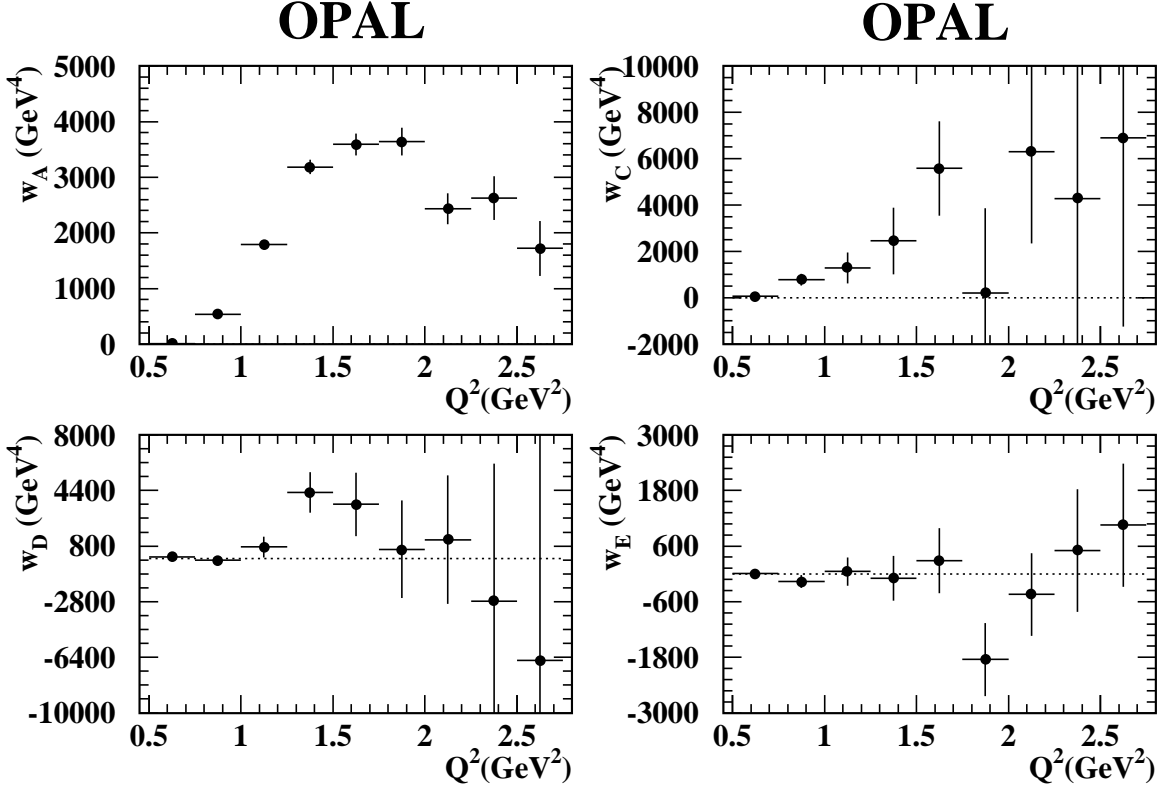


Figure 4: Measured structure functions w_A , w_C , w_D , and w_E as functions of Q^2 . Displayed are statistical errors only.

The detector effects and uncertainties in the detector simulation were estimated by varying the correction functions for the efficiencies within one standard deviation and increasing the width of the gaussians for the resolution simultaneously for all kinematic variables by 10 %. Furthermore P_τ has been varied within the errors [12]. As an additional check, data selected by the conventional cut method has been analyzed, leading to consistent results.

Table 3 summarizes the estimates of the different contributions to the systematic error averaged over all Q^2 bins. The variations from bin to bin are taken into account in table 2 where the measured values including statistical and systematic errors are given for each bin. The correlations between the values of the structure functions are typically ± 10 %.

5.2 Measurement of the parity violating asymmetry parameter γ_{VA}

As explained in section 4, the leptonic current depends on the parity violating asymmetry parameter γ_{VA} . A different γ_{VA} value therefore changes the result of the structure function measurement.

For the measurement of the hadronic structure functions described in the previous section the value of γ_{VA} was fixed to the Standard Model value $\gamma_{VA} = 1$. If γ_{VA} is instead

Q^2 (GeV ²)	N_j	w_A (GeV ⁴)			w_C (GeV ⁴)		
0.75 – 1.00	409	531	±30	±30	788	±250	±150
1.00 – 1.25	647	1790	±80	±70	1280	±670	±320
1.25 – 1.50	628	3190	±130	±130	2460	±1400	±480
1.50 – 1.75	413	3590	±200	±140	5580	±2000	±690
1.75 – 2.00	232	3640	±250	±200	198	±3700	±820
2.00 – 2.25	85	2430	±280	±150	6300	±4000	±2900
2.25 – 2.50	44	2630	±400	±140	4280	±6600	±1700
2.50 – 2.75	12	1720	±500	±180	6890	±8100	±8600
Q^2 (GeV ²)	N_j	w_D (GeV ⁴)			w_E (GeV ⁴)		
0.75 – 1.00	409	-115	±250	±90	-165	±130	±20
1.00 – 1.25	647	735	±670	±170	50	±300	±90
1.25 – 1.50	628	4270	±1300	±520	-94	±480	±90
1.50 – 1.75	413	3500	±2100	±830	284	±700	±450
1.75 – 2.00	232	595	±3200	±590	-1850	±790	±190
2.00 – 2.25	85	1210	±4200	±760	-444	±890	±310
2.25 – 2.50	44	-2760	±8900	±4100	504	±1300	±110
2.50 – 2.75	12	-6610	±15000	±4300	1050	±1300	±1100

Table 2: The hadronic structure functions for each Q^2 bin. For each structure function its central value (first column), statistical error (second column) and systematic error (third column) are given. N_j is the number of events in the given Q^2 bin. All contributions from table 3 are included in the systematic error.

	Δw_A	Δw_C	Δw_D	Δw_E
Background fraction	±1.5 %	±2.2 %	±5.9 %	±6.6 %
Kaon channels	±1.4 %	±20 %	±6.4 %	±14 %
Modelling of background	±3.0 %	±20 %	±30 %	±40 %
Efficiency	±4.0 %	±4.0 %	±5.7 %	±3.7 %
Detector resolution	< 0.1 %	±1.0 %	±2.0 %	±1.0 %
P_τ	< 0.1 %	±1.5 %	±2.5 %	±1.7 %

Table 3: Estimated contributions to the systematic error for the hadronic structure functions, averaged over the Q^2 bins.

varied in the fit the parity violating asymmetry parameter can be measured. The change in the likelihood function is shown in fig. 5, leading to a model independent measurement of $\gamma_{VA} = 1.08^{+0.46}_{-0.41} {}^{+0.14}_{-0.25}$, consistent with the Standard Model prediction of $\gamma_{VA} = 1$ for left-handed tau neutrinos. This result is in agreement with that of a model dependent analysis by ARGUS [2] using the same framework as this analysis (see also section 7.2), and also with

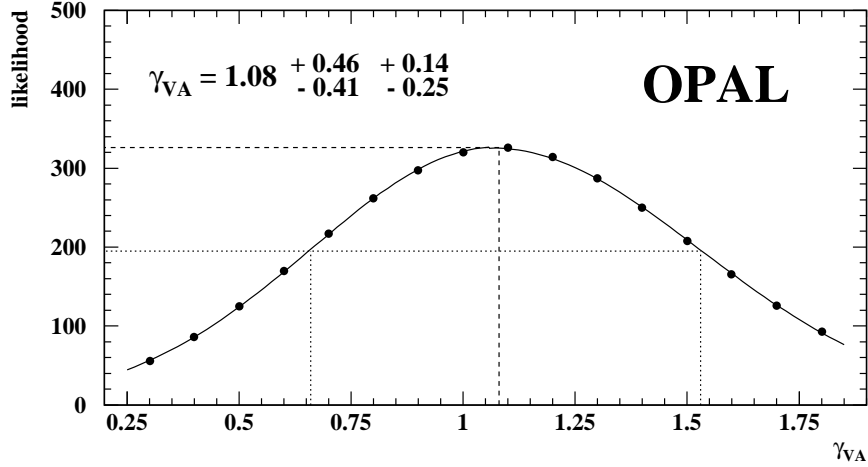


Figure 5: Change of the likelihood function dependent on γ_{VA} with a gaussian interpolation between the considered γ_{VA} values (points).

	$\Delta\gamma_{VA}$	$\Delta\gamma_{VA}^{\text{KS}}$	$\Delta\gamma_{VA}^{\text{IMR}}$
Background fraction	± 0.05	± 0.01	± 0.01
Kaon channels	-0.2	-0.03	-0.07
Modelling of background	± 0.05	± 0.03	± 0.03
Efficiency	± 0.1	± 0.03	± 0.03
Detector resolution	-0.05	$+0.01$	$+0.01$
P_τ	± 0.06	± 0.01	± 0.04
Variation of model parameters	—	± 0.02	± 0.11
Total systematic error	$^{+0.14}_{-0.25}$	$^{+0.05}_{-0.06}$	$^{+0.13}_{-0.14}$
Statistical error	$^{+0.46}_{-0.41}$	± 0.27	± 0.31

Table 4: Estimated error contributions for the γ_{VA} measurements: $\Delta\gamma_{VA}$ for the model independent measurement, $\Delta\gamma_{VA}^{\text{KS}}$ for the KS model and $\Delta\gamma_{VA}^{\text{IMR}}$ for the IMR model.

more recent helicity measurements of ALEPH and ARGUS with analyses based on other methods [21].

The systematic error is derived from the same variations as described in the previous section. The dominant effect comes from the uncertainty in the background, especially from 3-prong events with kaons in the final state. The error contributions are summarized in table 4. The values for the structure functions with $\gamma_{VA} = 1.08$ agree within the errors with the results given in section 5.1.

6 Model Descriptions of the Decay

Two models which describe the $\tau^- \rightarrow \pi^- \pi^- \pi^+ \nu_\tau$ decay will be investigated in this analysis. These are the models of Kühn and Santamaria [5] and of Isgur et al. [6], henceforth referred to as the KS model and IMR model, respectively. Both models describe the decay as proceeding primarily through the intermediate a_1 and ρ resonances, using Q^2 -dependent resonance widths and including interference effects from the two possible pion combinations that form the ρ . The mass and width of the a_1 resonance are parameters of both models that can only be determined from experimental data.

Integrating eq. (1) over the angles $(\cos \theta^*, \cos \beta, \gamma)$ and the Dalitz plot variables (s_1, s_2) leads to the expression for the decay rate [22]

$$\frac{d\Gamma(\tau^- \rightarrow \pi^- \pi^- \pi^+ \nu_\tau)}{dQ^2} = \frac{G_F^2 \cos^2 \theta_C}{16\pi m_\tau^3} (m_\tau^2 - Q^2)^2 [m_\tau^2 \rho_0(Q^2) + (m_\tau^2 + 2Q^2) \rho_1(Q^2)]. \quad (8)$$

The pseudoscalar and axial-vector spectral densities $\rho_0(Q^2)$ and $\rho_1(Q^2)$ are related to the hadronic structure functions by

$$\rho_0(Q^2) = \frac{1}{(4\pi)^4} \frac{1}{Q^4} w_{SA}, \quad (9)$$

$$\rho_1(Q^2) = \frac{1}{3} \frac{1}{(4\pi)^4} \frac{1}{Q^4} (w_A + w_B). \quad (10)$$

These expressions can be simplified under the assumptions introduced in section 4 ($w_B = 0$ and $w_{SA} = 0$). It is in the parametrization of $\rho_1(Q^2)$, and therefore w_A , where the KS and IMR models differ most significantly.

The IMR model employs strong form factors with full off-shell dependence, derived from a flux-tube breaking model [23]. These form factors are parameterized by a harmonic-oscillator strength β_{HO} and a string-breaking constant γ_0 . The model is formulated with two distinct $a_1 \rho \pi$ couplings which allows a prediction of the relative strengths of the two possible angular momentum states of the intermediate $\rho \pi$ state, the D/S ratio. The IMR model also allows for the a_1 to decay through the $K^* \bar{K}$ channel as well as a pseudoscalar contribution through $\pi(1300)$ production. Following the same assumptions made in section 4, however, the pseudoscalar contribution is not included in the present analysis, and so $\rho_0(Q^2) = 0$. Several effects, such as model deficiencies and possible non-resonant contributions are accounted for by employing a three parameter polynomial background term. In the IMR model, the width Γ_{a_1} of the a_1 resonance is not a free parameter, but rather is calculated from the a_1 mass and the form factors.

The KS model, in contrast, uses constant strong form factors [5]. The decay amplitude is formulated using the lowest dimensional Born term only. The Born term is not an orbital angular momentum eigenstate, but rather is a fixed admixture of angular momentum states. There is, therefore, no possibility to allow the D/S ratio to vary with the KS model⁵. The KS model is formulated with no pseudoscalar contribution. It does however allow for the a_1 to decay through the $\rho(1450)$ channel. Both the a_1 mass and width are free parameters of the KS model.

⁵With only the lowest dimensional Born term included, the D/S ratio is a function of kinematics only, with a weak dependence on the a_1 mass. Its value at $m_{a_1} = 1.266$ GeV is $D/S = -0.05$.

7 Analysis of the three-pion and two-pion mass distributions

Least-squares fits have been carried out to determine the a_1 mass and width for both the KS and IMR models. The distributions used for the measurements are the invariant 3π mass squared and three invariant 2π mass squared Dalitz-plot projections in different Q^2 intervals, shown in fig. 6 and 7. As indicated in fig. 7, the three Dalitz-plot projections are formed by cutting around the ρ mass in s_1 and then projecting onto s_2 , and vice versa, for three separate intervals in Q^2 . The background for each of the four histograms, represented by the hatched areas in fig. 6 and 7, is estimated by analyzing Monte Carlo simulated events, and is subtracted from each histogram before fitting. It should be pointed out that the Monte Carlo, which employs the KS model for the a_1 decay, overestimates the ρ peak in the Dalitz plot projections.

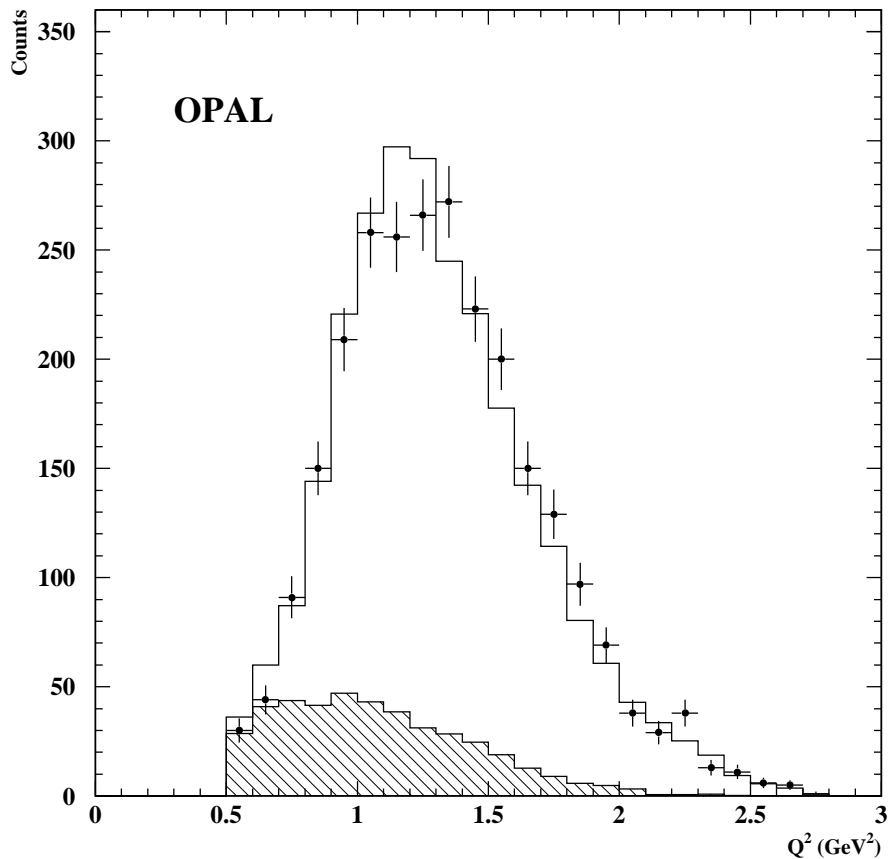


Figure 6: Distribution of the invariant 3π mass squared (Q^2) for data (points with error bars), Monte Carlo (solid line) and Monte Carlo background (hatched area).

Unless otherwise noted, all fits of the histograms with each model are performed simultaneously using all four histograms, thus allowing a complete investigation of correlations

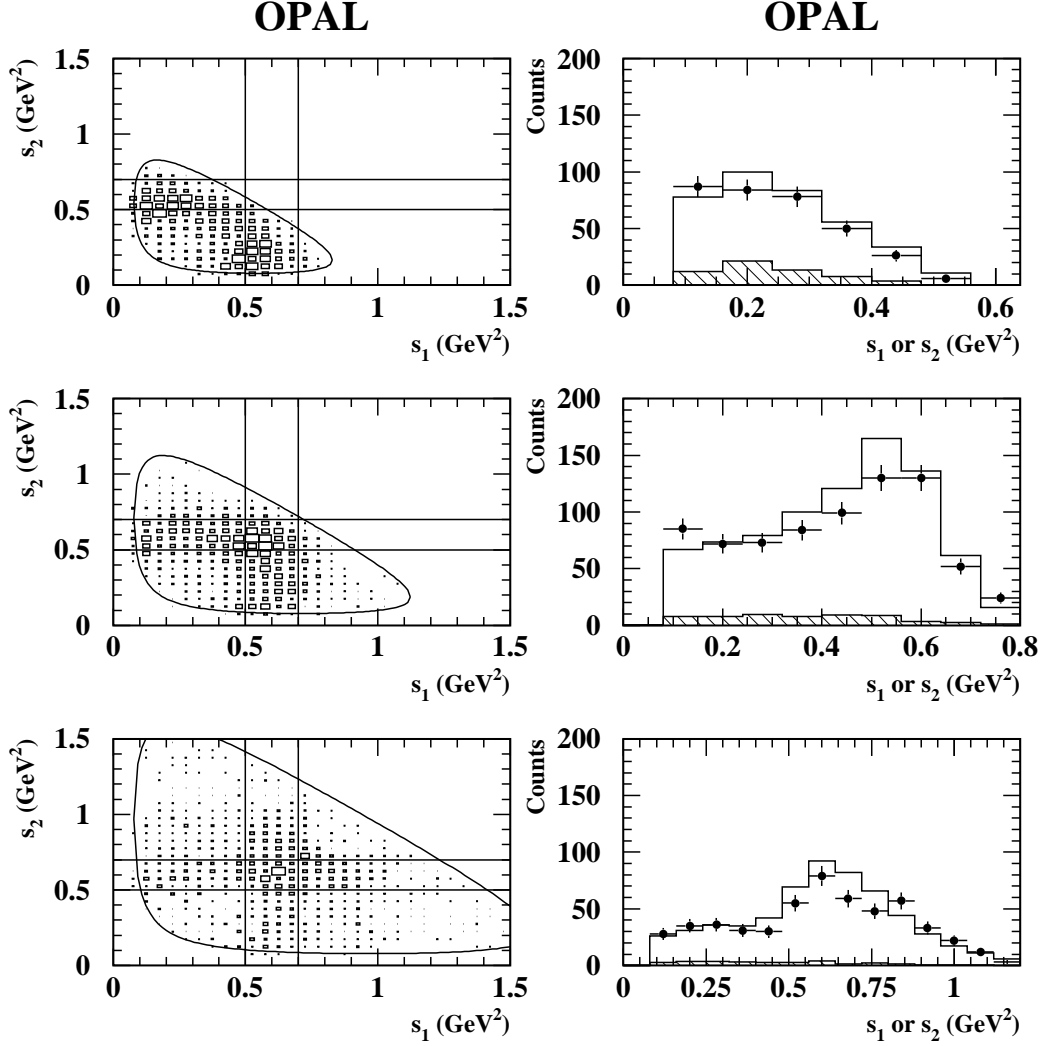


Figure 7: Dalitz plot distributions (s_1 vs s_2) are shown on the left for given intervals of Q^2 . To the right are the projections of the ρ -bands indicated in the Dalitz plots for data (points with error bars), Monte Carlo (solid line) and Monte Carlo background (hatched area). The limits of the ρ -bands are $0.5 < s_{1,2} < 0.7 \text{ GeV}^2$. Note that entries which fall within the overlap of the ρ -bands are counted in the projections twice. From top to bottom, the Q^2 intervals are $0.81 < Q^2 < 1.10 \text{ GeV}^2$, $1.10 < Q^2 < 1.44 \text{ GeV}^2$, and $1.44 < Q^2 < 1.96 \text{ GeV}^2$. The lack of agreement between the data and Monte Carlo is due to the implementation of the KS model in TAUOLA 2.4 [14] (see section 7.1).

among the various fit parameters and histograms. The overall normalization for each of the four histograms is constrained to be identical, and is taken as a free parameter of the fit. Since the absolute decay rate is not a subject of this analysis, the overall normalization has no physical significance.

	Kühn et al. [5]	Isgur et al. [6]
m_{a_1} (GeV)	$1.266 \pm 0.014_{-0.002}^{+0.012}$	$1.202 \pm 0.009_{-0.001}^{+0.009}$
Γ_{a_1} (GeV)	$0.610 \pm 0.049_{-0.019}^{+0.053}$	$0.422 \pm 0.023_{-0.004}^{+0.033}$
D/S ratio	—	$-0.09 \pm 0.03 \pm 0.01$
$\chi^2/d.o.f.$	62.2/48	44.1/44

Table 5: Model parameters extracted from fitting the KS and IMR models to OPAL data. The errors quoted are statistical, followed by systematic. Note that Γ_{a_1} and the D/S ratio for the IMR model are calculated quantities, not parameters of the fit.

For the fits with the KS model, the free parameters of the fit are the a_1 mass m_{a_1} , the a_1 width at the pole $\Gamma_{a_1}(m_{a_1}^2)$, and the overall normalization. The $\rho(1450)$ is included in the KS model parametrization with a strength $\beta_{\rho(1450)} = -0.145$, as specified for model 1 of table 1 in ref. [5].

As pointed out previously, it is possible to extract the D/S ratio with the IMR model. This is accomplished in the present analysis by allowing the strengths of the $f_{a_1\rho\pi}$ and $g_{a_1\rho\pi}$ form factors (see ref. [6]) to vary independently from their nominal flux-tube breaking model values. The relative strengths of these two form factors are most sensitive to the shapes of the three Dalitz-plot projections. All other form factor parameters are held fixed at their nominal values, $\beta_{HO} = 0.4$ GeV and $\gamma_o = 0.39$. For the fits to the data with the IMR model, the free parameters of the fit are the a_1 mass, the overall normalization, the three parameters which govern the strength and shape of the polynomial background underlying the 3π distribution, and the two strengths for the $f_{a_1\rho\pi}$ and $g_{a_1\rho\pi}$ form factors. It should be noted that the overall normalization is applied only to the part of the invariant 3π mass squared histogram lying above the polynomial background. The $K^*\bar{K}$ decay channel is allowed to contribute to the total decay width.

Both selection efficiency and OPAL detector resolution are estimated for this analysis by analyzing Monte Carlo simulated events. The selection efficiency is accounted for by dividing, bin by bin, the background-subtracted data by the estimated selection efficiency curve. The data for each histogram is then renormalized by multiplying the contents of each bin by the efficiency averaged over the histogram. Errors in the efficiency are combined with the Monte Carlo simulated background statistical errors and the data statistical errors for each bin to yield total errors for the fitting procedure. The detector resolution is accounted for by folding into the fit function the estimated resolution function.

7.1 Results

The results of the fits with each of the models are shown in fig. 8 and are summarized in table 5. As can be seen from fig. 8, the KS model gives a good description of the shape of the Q^2 distribution, although the fit can be seen to be consistently low over most of the distribution. As a check, the Q^2 distribution was also fitted separately. The fitted parameters were consistent with those of the four-histogram fit, and the χ^2 was 20.8 for 19 *d.o.f.* The

2π mass projections are also reasonably well described by the model, although the relative ρ peak contribution is overestimated and the low $s_{1,2}$ region is underestimated.

The IMR model, as can be seen in fig. 8, gives a good description of the Q^2 distribution. The polynomial background term employed by the IMR model serves to correct for the nor-

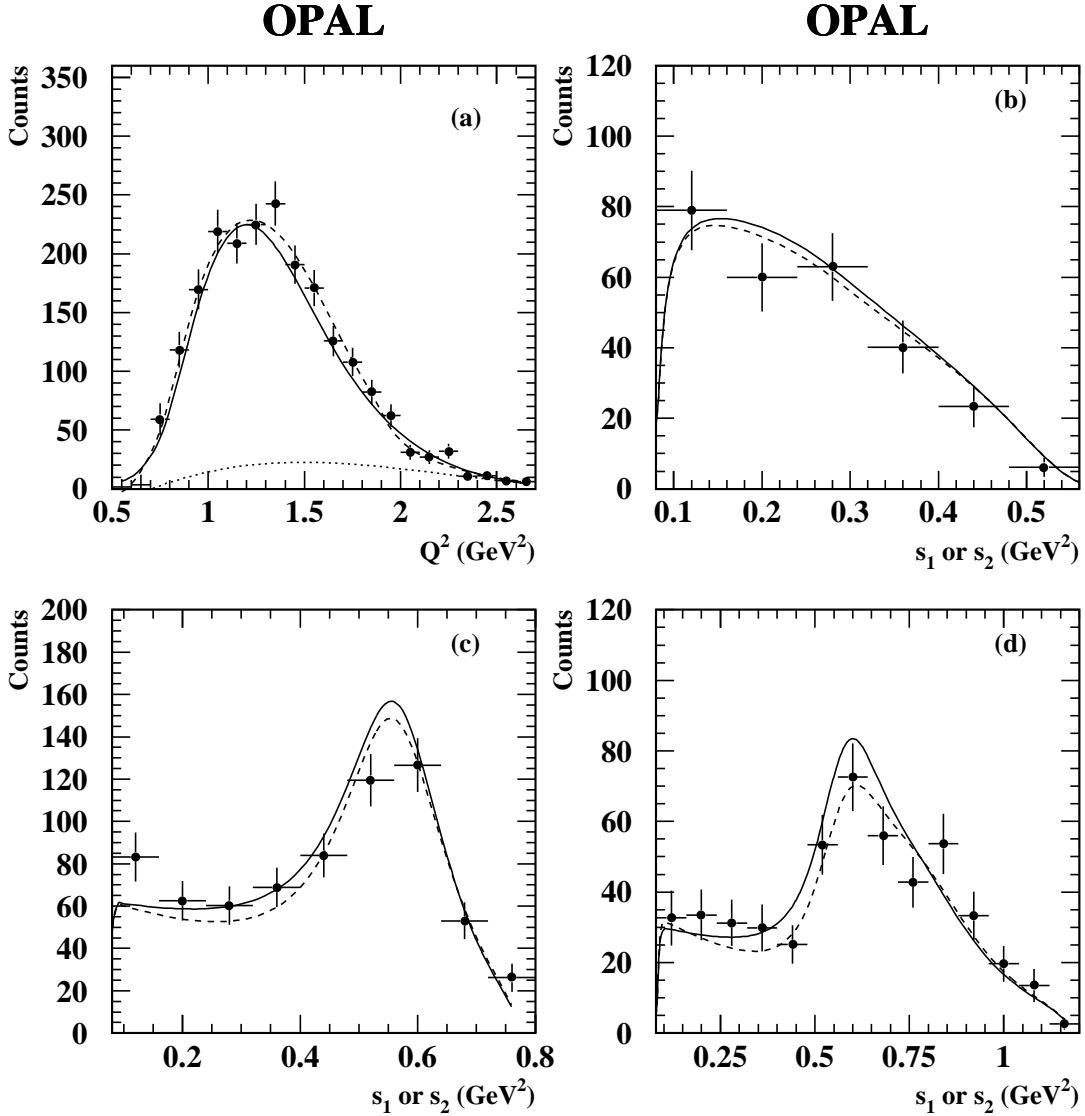


Figure 8: The model fits to the data. The data shown have been corrected for background and efficiency. The detector resolution is folded into the models. The solid line is the KS model fit and the dashed line is the IMR model fit. The dotted line under the 3π distribution is the polynomial background of the IMR model. The Q^2 intervals are (b) $0.81 < Q^2 < 1.10$ GeV², (c) $1.10 < Q^2 < 1.44$ GeV², and (d) $1.44 < Q^2 < 1.96$ GeV².

	KS model error		IMR model error		
	Δm_a (GeV)	$\Delta \Gamma_a$ (GeV)	Δm_a (GeV)	$\Delta \Gamma_a$ (GeV)	$\Delta D/S$
Kaon channels	+0.011	+0.042	+0.006	+0.024	-0.01
Modelling of background	+0.005	+0.027	+0.007	+0.023	-0.01
Background fraction	± 0.002	± 0.019	± 0.001	± 0.004	< 0.01
Detector resolution	± 0.001	± 0.002	< 0.001	± 0.001	< 0.01
Total systematic error	$+0.012$ -0.002	$+0.053$ -0.019	$+0.009$ -0.001	$+0.033$ -0.004	± 0.01
Statistical error	± 0.014	± 0.049	± 0.009	± 0.023	± 0.03

Table 6: Estimated error contributions for each of the KS and IMR model fits.

malization problem seen with the KS model fit. However, if the polynomial background is excluded from the IMR model, the χ^2 increases to 74.9 for 47 *d.o.f.* and the extracted parameters shift significantly. The three parameters for the polynomial background of the IMR fit are $c_1 = -7.3$, $c_2 = 14.9$, and $c_3 = -1.9$ (see [6] for the parametrization of the polynomial background). These three parameters are highly correlated and have errors ranging from 50% to 190%. The normalization is such that the background contribution is 13.7% of the total 3π distribution.

The 2π mass projections are also well described by the IMR model, with a slight improvement over the fit by the KS model. However the systematic problems noted above regarding the ρ peak contribution and the low $s_{1,2}$ region are present with the IMR model fit also. It should be noted that these shortcomings of the models have been observed before by ARGUS [2] and seem to warrant further theoretical work towards a better modeling of the $\tau^- \rightarrow \pi^- \pi^- \pi^+ \nu_\tau$ decay.

The results for the strong decay on-shell $a_1\rho\pi$ form factors and the D/S ratio of the IMR model fit are $f_{a_1\rho\pi}(m_{a_1}^2, m_\rho^2) = 4.8 \pm 0.2$ GeV, $g_{a_1\rho\pi}(m_{a_1}^2, m_\rho^2) = 3.2 \pm 2.0$ GeV, and $D/S = -0.09 \pm 0.03 \pm 0.01$. These values are in reasonable agreement with the predictions of the flux-tube breaking model [6].

Table 6 summarizes the systematic errors on the a_1 resonance parameters. Several checks were made concerning the background. The effects of removing the cut against kaons and the effects of using TAUOLA 1.5 [18] to model the background were investigated. For these two variations, half of the change from the nominal fits is taken as the error. The background fraction was also varied by ± 0.02 from the nominal value of $f_{bgd} = 0.175$. The effects of the detector resolution were investigated by varying the mass resolution by $\pm 10\%$. This has a negligible effect on the extracted parameters. The data selected by the conventional cut method was also fitted with both models, with results consistent with those obtained above.

7.2 Comparison of the Structure Functions to the Model Predictions

In fig. 9 the measured structure functions from section 5.1 are compared to the KS and IMR model predictions using the fit parameters extracted in the previous section. For the

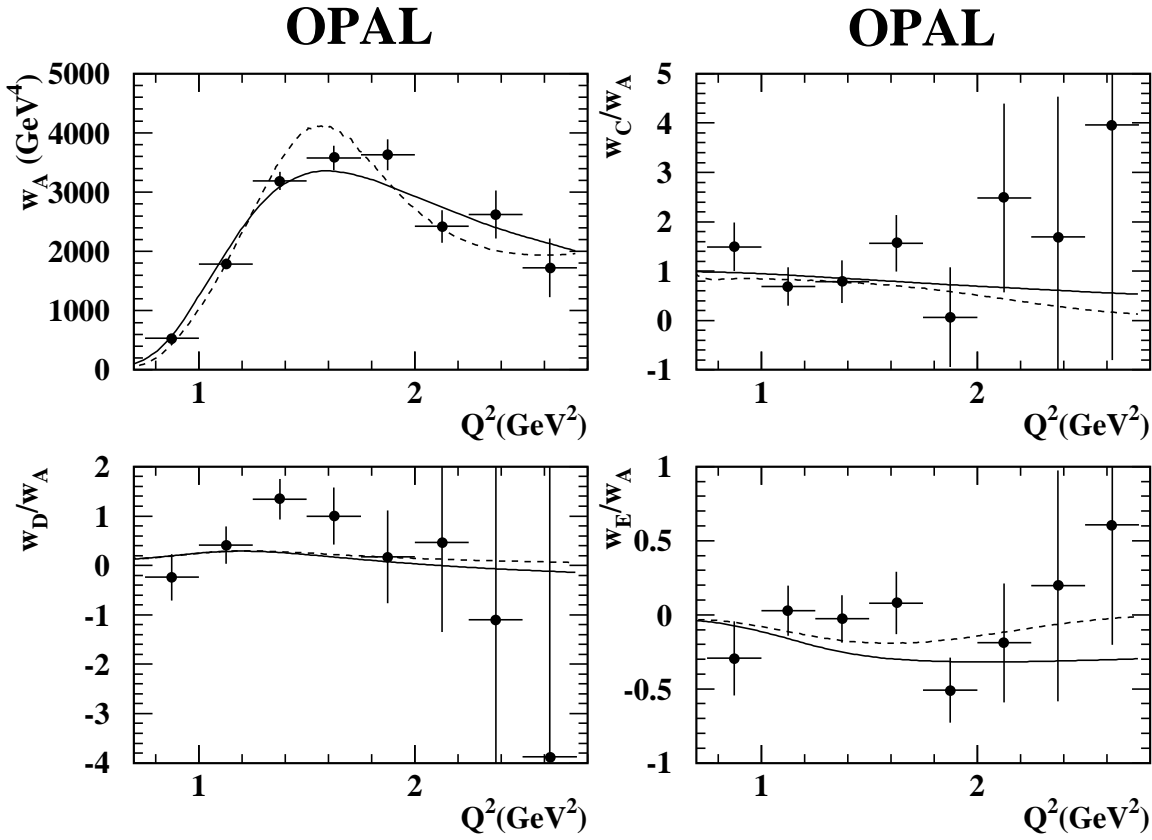


Figure 9: Comparison of the measured structure functions (points with error bars) with the models of Isgur et al. (dashed line) [6] and Kühn et al. (solid line) [5]. The IMR model prediction for w_A includes the polynomial background term.

IMR model the polynomial background term is included in w_A . The model predictions are normalized such that the total cross sections derived from the integration of eq. (8) for the model predictions and the measured structure functions agree with one another. The ratio w_X/w_A , which is independent of the normalization and only weakly dependent on m_{a_1} and Γ_{a_1} , is plotted for each of the other three structure functions. Both models describe the data well. The χ^2 of the data with respect to the KS model is 42 for 32 bins, and 39 for 32 bins for the IMR model.

A fit to γ_{VA} is performed by replacing the fit parameters w_X^j in eq. (4) by the hadronic structure functions derived from the two models. The model dependent value obtained for the parity violating asymmetry parameter is $\gamma_{VA} = 0.87 \pm 0.27^{+0.05}_{-0.06}$ for the KS model and $\gamma_{VA} = 1.10 \pm 0.31^{+0.13}_{-0.14}$ for the IMR model. The systematic errors have been derived from the same variations as described in section 5 and by varying the model parameters within the errors given in section 7.1. A summary of the different contributions is given in table 4. The largest systematic error contribution for the IMR model is due to the uncertainty in the D/S ratio. No variation of this parameter is possible with the KS model.

8 Conclusions

We have studied the structure of the decay $\tau^- \rightarrow \pi^- \pi^- \pi^+ \nu_\tau$ using two different approaches. First, a model independent measurement of the four structure functions w_A , w_C , w_D , and w_E has been presented. The model independent value for the parity violating asymmetry parameter has been determined to be

$$\gamma_{VA} = 1.08^{+0.46}_{-0.41} {}^{+0.14}_{-0.25},$$

consistent with the Standard Model prediction of $\gamma_{VA} = 1$ for left-handed tau neutrinos. Second, the models of Kühn and Santamaria and of Isgur et al. have been used to fit the distributions of the invariant 3π mass as well as 2π mass projections of the corresponding Dalitz plot. Both models describe well the shape of the 3π mass squared distribution, although the Kühn and Santamaria model is slightly low over most of the distribution. The description by both models of the 2π mass projections is satisfactory, with the exception that both models overestimate the ρ peak and underestimate the low $s_{1,2}$ region. The results obtained for the a_1 resonance model parameters and the parity violating asymmetry parameter for the Kühn and Santamaria model are

$$\begin{aligned} m_{a_1} &= 1.266 \pm 0.014^{+0.012}_{-0.002} \text{ GeV} \\ \Gamma_{a_1} &= 0.610 \pm 0.049^{+0.053}_{-0.019} \text{ GeV} \\ \gamma_{VA} &= 0.87 \pm 0.27^{+0.05}_{-0.06}. \end{aligned}$$

For the Isgur et al. model, the results obtained are

$$\begin{aligned} m_{a_1} &= 1.202 \pm 0.009^{+0.009}_{-0.001} \text{ GeV} \\ \Gamma_{a_1} &= 0.422 \pm 0.023^{+0.033}_{-0.004} \text{ GeV} \\ D/S &= -0.09 \pm 0.03 \pm 0.01 \\ \gamma_{VA} &= 1.10 \pm 0.31^{+0.13}_{-0.14}. \end{aligned}$$

Acknowledgements

We would like to thank J. H. Kühn and E. Mirkes for many useful discussions.

It is a pleasure to thank the SL Division for the efficient operation of the LEP accelerator, the precise information on the absolute energy, and their continuing close cooperation with our experimental group. In addition to the support staff at our own institutions we are pleased to acknowledge the

Department of Energy, USA,

National Science Foundation, USA,

Particle Physics and Astronomy Research Council, UK,

Natural Sciences and Engineering Research Council, Canada,

Fussefeld Foundation,

Israel Ministry of Science,

Israel Science Foundation, administered by the Israel Academy of Science and Humanities,

Minerva Gesellschaft,

Japanese Ministry of Education, Science and Culture (the Monbusho) and a grant under the Monbusho International Science Research Program,

German Israeli Bi-national Science Foundation (GIF),
Direction des Sciences de la Matière du Commissariat à l'Energie Atomique, France,
Bundesministerium für Forschung und Technologie, Germany,
National Research Council of Canada,
A.P. Sloan Foundation and Junta Nacional de Investigação Científica e Tecnológica, Portugal.

Appendix

A Leptonic Functions L_X

The four leptonic functions L_X for the measurement of the decay $\tau^- \rightarrow \pi^- \pi^- \pi^+ \nu_\tau$ described in this paper can be written as:

$$\begin{aligned} L_A &= \frac{2}{3}K_1 + K_2 + \frac{1}{3}\overline{K}_1 (3 \cos^2 \beta - 1)/2 \\ L_C &= -\frac{1}{2}\overline{K}_1 \sin^2 \beta \cos 2\gamma \\ L_D &= \frac{1}{2}\overline{K}_1 \sin^2 \beta \sin 2\gamma \\ L_E &= Q_{q_3} \overline{K}_3 \cos \beta \end{aligned}$$

with

$$\begin{aligned} K_1 &= 1 - \gamma_{VA} P_\tau \cos \theta^* - (m_\tau^2/Q^2)(1 + \gamma_{VA} P_\tau \cos \theta^*) \\ K_2 &= (m_\tau^2/Q^2)(1 + \gamma_{VA} P_\tau \cos \theta^*) \\ K_3 &= \gamma_{VA} - P_\tau \cos \theta^* \\ K_4 &= \sqrt{m_\tau^2/Q^2} \gamma_{VA} P_\tau \sin \theta^* \\ K_5 &= \sqrt{m_\tau^2/Q^2} P_\tau \sin \theta^* \\ \overline{K}_1 &= K_1(3 \cos^2 \psi - 1)/2 - \frac{3}{2}K_4 \sin 2\psi \\ \overline{K}_2 &= K_2 \cos \psi + K_4 \sin \psi \\ \overline{K}_3 &= K_3 \cos \psi - K_5 \sin \psi \end{aligned}$$

where

$$m_\tau = 1.7771 \text{ GeV [12]},$$

$P_\tau = -0.142 \pm 0.006$, P_τ taken here from a calculation of the electroweak parameters out of M_Z , m_t and M_H depending only weakly via m_t on the P_τ measurement [12],

$\gamma_{VA} = 2g_V g_A / (g_V^2 + g_A^2)$ is the parity violating asymmetry parameter ($g_V = g_A = 1$ in the Standard Model),

Q^2 is the invariant mass of the hadronic system,

β, γ, θ^* as defined in section 4,

ψ is the angle between the boost direction and the direction of flight of the τ as seen from the hadronic rest frame,

Q_{q_3} is the sign of the charge of the unlike-sign pion (+1 for a τ^- decay).

For the full set of leptonic functions see ref. [4].

References

- [1] G. Alexander et al., PLUTO coll.: Phys. Lett. 73B (1978) 99.
- [2] H. Albrecht et al., ARGUS coll.: Z. Phys. C 58 (1993) 61.
- [3] D. Buskulic et al., ALEPH coll.: Z. Phys. C 59 (1993) 369.
- [4] J. H. Kühn and E. Mirkes, Z. Phys. C 56 (1992) 661.
- [5] J. H. Kühn and A. Santamaria, Z. Phys. C 48 (1990) 445.
- [6] N. Isgur, C. Morningstar and C. Reader, Phys. Rev. D 39 (1989) 1357.
- [7] K. Ahmet et al., OPAL coll.: Nucl. Inst. Meth. A 305 (1991) 275;
P.P Allport et al., OPAL coll.: Nucl. Inst. Meth. A 324 (1993) 34;
P.P Allport et al., OPAL coll.: Nucl. Inst. Meth. A 346 (1994) 476.
- [8] O. Biebel et al., Nucl. Inst. Meth. A 323 (1992) 169.
- [9] M. Z. Akrawy et al., OPAL coll.: Phys. Lett. B 247 (1990) 458.
- [10] R. Akers et al., OPAL coll.: CERN-PPE/95-06.
- [11] R. Akers et al., OPAL coll.: CERN-PPE/94-171.
- [12] Particle Data Group, Phys. Rev. D 50 (1994) 1173.
- [13] S. Jadach, B. F. L. Ward and Z. Wąs, Comput. Phys. Commun. 79 (1994) 503.
- [14] S. Jadach, Z. Wąs, R. Decker and J. H. Kühn, Comput. Phys. Commun. 76 (1993) 361.
- [15] J. Allison et al., Nucl. Inst. Meth. A 317 (1992) 47.
- [16] M. Jacob, Il Nuovo Cimento 9 (1958) 826.
- [17] R. J. Barlow: Statistics. New York: John Wiley & Sons (1989).
- [18] S. Jadach, J. H. Kühn and Z. Wąs, Comput. Phys. Commun. 64 (1991) 275.
- [19] H. Albrecht et al., ARGUS coll.: Phys. Lett. B 260 (1991) 259.
- [20] P. Baringer et al., CLEO coll.: Phys. Rev. Lett. 59 (1987) 1993.
- [21] D. Buskulic et al., ALEPH coll.: Phys. Lett. B 321 (1994) 168;
H. Albrecht et al., ARGUS coll.: Phys. Lett. B 337 (1994) 383;
D. Buskulic et al., ALEPH coll.: CERN-PPE/94-209;
H. Albrecht et al., ARGUS coll.: DESY/95-011.
- [22] Y.S. Tsai, Phys. Rev. D 4 (1971) 2821.
- [23] R. Kokoski and N. Isgur, Phys. Rev. D 35 (1987) 907.